Instantaneous 3D-imaging of highly turbulent flames using Computed Tomography of Chemiluminescence (CTC)

KHADIJEH MOHRI[1,*], SIMON GÖERS[2], JONATHAN SCHÖLER[2], ANDREAS RITTLER[1], THOMAS DREIER[2], CHRISTOF SCHULZ[2], AND ANDREAS KEMPF[1]

[1] Institute for Combustion and Gas Dynamics (IVG), Fluid Dynamics, University of Duisburg-Essen, 47057, Duisburg, Germany
[2] IVG, Reactive Fluids, University of Duisburg-Essen, 47057, Duisburg, Germany
[*] Corresponding author: khadijeh.mohri@uni-due.de

Compiled July 25, 2017

The CTC technique was applied for the first time to a real highly turbulent swirl flame setup, using a larger number of CCD cameras ($N_q = 24$ views), to directly reconstruct the three-dimentional (3D) instantaneous and time-averaged checmilumienscence fields. The views were obtained from a 172.5° region (in one plane) around the flame, and the CTC algorithm (Floyd et al., Combust. Flame 158, 2011) was used to reconstruct the flame by discretising the domain into voxels. We investigated how the reconstructions are affected by the views' arrangement and settings of the algorithm, and considered how the quality of reconstructions should be assessed to ensure a realistic description of the technique's capabilities. The reconstructions using $N_q \leq 12$ were generally better when the cameras were more equiangularly distributed. When N_q was severely low (e.g. 3), the reconstruction could be improved by using less voxels. The paper concludes with a summary of the strengths and weaknesses of the CTC technique for examining a real turbulent flame geometry and provides guidance on best practice.

OCIS codes: *(100.6950) Tomographic image processing; (120.1740) Combustion diagnostics; (280.2470) Flames; (110.6955) Tomographic imaging.*

http://dx.doi.org/10.1364/ao.XX.XXXXXX

1. INTRODUCTION

Most practical flames are unsteady, turbulent, and three-dimensional. In order to achieve fundamental insight into the nature of turbulent and unsteady flames, an accurate measurement of the temporal three-dimensional (3D) flame structure is desirable. Such measurements can aid in revealing the topology of turbulent flames and characteristics of unsteady flames in various applications. With increased knowledge of turbulent and unsteady flames it would be possible to improve on existing combustion devices, such as burners, which can for example aid in reduction of harmful emissions. Effort has been made to develop techniques for the study of the three-dimensional structure of a range of flames over the years, and one promising technique that is relatively recent is computed tomography (CT).

Many of the existing techniques provide either time-averaged, e.g. Phase Doppler Analysers, spatially averaged information by line-of-sight measurements, or information from pre-selected planes only, e.g., Planar Laser-Induced Fluorescence imaging. While time-resolved volumetric measurements of species and temperature are in principle possible with scanning lasers and using high-speed cameras, the equipment is extremely expensive and challenging to use in turbulent flames. On the other hand, non-intrusive diagnostic measurements based on flame chemiluminescence can be combined with tomographic reconstruction, such as the CTC, to directly provide 3D information with comparatively simpler and less expensive arrangements.

Although tomographic reconstruction can be strongly associated with medical applications originating from the 1970s, that were based on X-ray detection, it has been applied in other fields over the years. X-ray CT has been developed in several industries including electrical and electronic devices, food industry, inhomogeneous materials and the manufacturing industry for quality control purposes [1]. In the field of engineering, CT has been realised by several researchers, based on different measurement techniques such as schlieren [2], PIV [3], laser absorption [4], laser-induced fluorescence [5], and natural emissions such as chemiluminescence [6–16]. In the combustion community, Hertz and Faris [16] are recognised for using CT on flames for the first time.

With the CT technique, the local three-dimensional field of a

scalar quantity can be reconstructed using multiple line-of-sight integrated measurements that are obtained from different angles around the object under study. Combined with measurements of the naturally occurring flame chemiluminescence, the light emitted from excited species such as CH*, OH*, CO_2* and C_2*, would give a measure of the flame geometry, with OH* and CH* being prominent markers for the reaction zone. Spatially-resolving the flame's chemiluminescence field can help investigate important flame features such as propagation and wrinkling, vortex shedding and breakdown, and jet precession and recirculation. Additionally, it can provide useful data for the improved validation of advanced numerical simulations, for example on flame curvature or flame surface density.

Recently, Anikin et al. [11] showed that the tomographic reconstruction of two-dimensional OH*-chemiluminescence fields is useful for the detailed investigation of turbulent combustion. Worth and Dawson [8] followed by using tomographic reconstruction of OH*-chemiluminescence to reveal the complex 3D flame structures that are formed through collision of the large-scale vortex-flame structures along the shear layer of two interacting turbulent premixed flames. Most recently, Ma et al. [17] demonstrated the feasibility of high-speed chemiluminescence tomography for quantification of the flame surface shape to resolve the dynamics of turbulent flames.

Computed Tomography of Chemiluminescence (CTC) [12, 13, 18], is based on the Algebraic Reconstruction Technique (ART), and was first introduced by Floyd et al. [13] in a format where the flame's chemiluminescence field is reconstructed directly in 3D. The main features of a premixed CH_4/air turbulent opposed jet (TOJ) flame were resolved through reconstructions with the CTC, using simultaneous views from ten directions and a camera exposure time of 0.25 ms [13]. Furthermore, Floyd et al. [12] demonstrated high-resolution three-dimensional reconstructions of the CH*-chemiluminescence field for a CH_4/O_2 matrix burner, consisting of 21 laminar diffusion jet flames that exhibit multiple flame fronts. The reconstructions, using 48 non-instantaneous views that were obtained by moving one camera around the steady flames, were in good agreement with the observed flame shape and resolved structures of approximately 220 μm, over a domain width of 22 mm. The spatial resolution was determined by using phantoms that contained structures of known sizes [13, 18].

Some of the challenges involved with applying CTC to combustion environments include the need to obtain instantaneous measurements simultaneously, since in almost all cases the flame is unsteady, using the maximum number of views possible, to obtain better reconstructions. Increasing the number of views calls for finding a low-cost solution, such as using commodity cameras (as possible with the CTC technique) instead of very expensive high-spec cameras. The total number of views that is practically achievable is also often limited (at least for practical flames in internal combustion engines or gas-turbine combustors), and in many cases the views might be obstructed. For coping with limited views, ART-based algorithms, which may incorporate *a priori* information for improved reconstructions, have proven to work relatively well [12, 13, 19]. The computational cost of running a tomographic algorithm, especially when high-speed measurements are required for resolving the temporal variations inherent in turbulent and unsteady flames, can also pose a challenge.

In the current work, we have applied our CTC technique to the turbulent TECFLAM swirl burner [20–23]. The swirl burner is an excellent source of varying turbulent structures and a good representation of flames in swirled premixed combustion in gas turbines, and of flames in other industries. Reconstructing the 3D shape of this flame is challenging and our aim is to demonstrate the capability of CTC as applied to a real flame setup using a large number of cameras, and to address some of the important practical aspects that can affect the reconstructions. We illustrate how the locations of the views influence the reconstructions, and we present a systematic study of different view configurations in one plane. We also discuss the effect of the number of voxels that are used to discretise the 3D flame domain.

2. THE CTC TECHNIQUE

Our CTC system constitutes a number of detector units (camera and lens) and an accompanying CT algorithm that is used to reconstruct the intensity field. The CT algorithm originates from the work of Floyd [12, 13, 18]. The chemiluminescence intensity field is calculated using projection measurements, in the form of camera images, that are obtained simultaneously from multiple cameras at different viewing angles θ around the flame. As shown in figure 1, a view constitutes a set of projections N_p (the total number of pixels in one camera image) that are obtained at the same angle θ. A total number of N_q views are used to reconstruct the flame, which in principle can be considered as a 3D scalar field in the form of $Q(x, y, z)$. The prominent excited species that have been detected with our system (CH* and C_2*) are illustrated by the emission spectrum and the cameras' spectral response curves, as presented and discussed later in section 4 (figure [5)] (the broadband CO_2* is not labelled on this figure). It is noteworthy that since the individual reactions vary independently throughout the flame, if the broadband signal is detected then the relationship between the local heat release rate and Q is variable. This gives rise to uncertainty about the local heat release rate and would be a shortcoming of broadband CTC if quantitative flame data are sought.

The chemiluminescence distribution can be related to optical measurements via the radiative transfer equation (RTE), which results in a Fredholm integral equation of the first kind (IFK) [24], and can be approximated by a summation over a finite basis (e.g., voxels within a uniform Q, as given in equation 1). The RTE was simplified for the CTC by subtracting the background signal and neglecting scattering and re-absorption. The discrete approximation of the RTE is generated by discretising the flame domain into 3D voxels, as shown in figure 1, and by approximating the projection measurement I_{iv} as a finite sum going through the 3D field.

$$I_{iv} = \sum_{v=1}^{N_v} (w_i Q_v) \tag{1}$$

In equation 1, i and v refer to the line-of-sight projection and a voxel, respectively. w_i represents the contribution of each voxel to the line-of-sight projection. The effect of the camera optics was implemented by Floyd [18] when determining w_i for each projection to account for the depth-of-field. This was achieved by considering a simplified version of the camera optics using ray-tracing, that allows the propagation of a spherical light wave to be represented by a number of rays that are traced through the optical system, assuming that the camera aperture is much larger than the wavelength of the light. The paraxial approximation (that the angles made by any traced rays with the optical axis are small, i.e., $\tan(\theta) \approx \theta$) was also assumed, and is valid since the distance of the object to the lens is almost always much

larger than the camera aperture. The ray-tracing approach for modeling optical projections has been used previously, for example by Walsh et al. [25]. Non-parallel projections were also implemented to help account for perspective effects. The projected rays of a view will form different angles to the optical axis, depending on the distance of the object to the lens and the object's diameter. When the object distance relative to the object diameter is large, the rays can be assumed to be parallel, but as the object distance reduces the assumption of parallel rays becomes less valid. The detailed description of the projections considering the camera optics and non-parallel rays in the CTC algorithm can be found in [18].

The 3D discretisation in our CTC algorithm allows for out-of-plane views to be considered. The viewing direction relative to the central plane is described by an inclination angle γ, see figure 1. In every iteration step the measured projection I_{iv} is compared with an equivalent projection that is taken through the current iteration's estimate of the object $Q^{(h)}$, where h denotes the current iteration. The reconstruction is assumed to be converged once the absolute difference of the sum of the field vector, from one iteration to the next, is below the threshold $\Delta_c \times Q^{(h)}$ [19]. The accuracy and resolution of the reconstructions are affected by several factors, for example the resolution and number of views and the exact description of the location and orientation of the views [13, 18]. More information and detail about the algorithm is available from Floyd [12, 13].

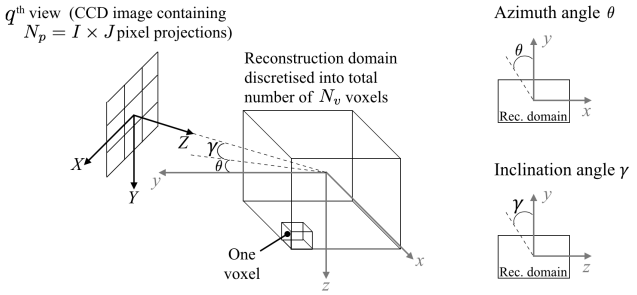

Fig. 1. View and 3D reconstruction coordinates definition

3. THE GENERAL CTC SETUP

A maximum number of $N_q = 24$ CCD cameras were positioned within a 172.5° region around the target flame, as shown in figure 2. The angular separation between each camera, in the horizontal plane, was $\theta = 7.5°$. The cameras were mounted on a single base plate with pre-set holes at a fixed distance to the flame and the aforementioned angular separation. In the work presented here, the cameras were placed in one plane ($\gamma = 0$), and images perpendicular to the flow direction were obtained. To align the cameras a back-illuminated pinhole structure, that was mounted on a rotation stage that can measure the angle to an accuracy of $\pm\, 0.5^o$, was placed coaxially on the centre of the burner. The cameras were then aligned such that an image of the light point would fall on the centre pixel of the camera image.

The cameras used were Basler acA645-100gm, featuring a $\frac{1}{2}''$ Sony ICX414 monochrome sensor with 659 by 494 pixels of size 9.9×9.9 μm. The peak spectral response of the cameras, at $> 60\%$, is between about 400 and 680 nm. Kowa C-mount lenses, with a focal length of 12 mm, were mounted on the cameras. Since the cameras were UV-insensitive, this study focused on the visible part of the emitted chemiluminescence

Fig. 2. The tomography setup around the swirl burner, showing 24 cameras with filters arranged around the burner.

and on gathering as much intensity as possible. Filters (Schott BG40) to suppress the detection of light emission attributed to hot H_2O were found to be necessary, as explained in section 4. All cameras received the same TTL signal from one trigger source, while the setup and the readout of the cameras was done through two Ethernet switches (Gigabit smart TL-SG2424P) that also provided the electrical power, and were connected to the control and evaluation computer.

The camera exposure time was chosen based on a compromise between minimising motion blur and maintaining adequate signal-to-noise ratio SNR (for example $SNR = 18$ for equivalence ratio $\phi = 1.0$ and $t_{\text{exp}} = 0.4$ ms, Flame I in table 1). This was achieved by running several trial tests to find the optimum. To achieve appropriate SNR values, the largest aperture opening, $f/1.4$, was needed. The total depth of field in this case would be 53 mm, assuming a circle of confusion of 0.02 mm. A measure of the level of focus at the far ends of the burner exit was made. Images of a target, two neighbouring squares (one black and one white), were obtained by placing it at the rim of the swirl burner exit closest to the cameras (front) and furthest away from the cameras (back). The signal intensity across the black and white squares was used to plot the Line Spread Function (LSF), from which the full-width-half-maximum (w), which is the width of the LSF curve where the signal drops to half the maximum value, was calculated for all the cameras. The average of the minimum full-width-half-maximum $w_{\text{min-avg}}$ was calculated from images of the target at the plane onto which the cameras were actually focused. The ratio of the average w at the front and back locations ($w_{\text{front}-\text{avg}}$ and $w_{\text{back}-\text{avg}}$) to $w_{\text{min}-\text{avg}}$ was found to be $(w_{\text{front}-\text{avg}}/w_{\text{min}-\text{avg}}) = 1$ and $(w_{\text{back}-\text{avg}}/w_{\text{min}-\text{avg}}) = 1.2$. As outlined in section 2, the limited depth-of-field is accounted for in the CTC algorithm. The CCD pixel size is taken as an approximation for the area of acceptable blur, i.e., circle of confusion.

A black background, viewable by all cameras, was placed behind the flames for improved flame image quality. Background correction was applied to all images prior to the reconstructions. This was achieved by obtaining an image with each camera without the flame in operation to capture the background signal. The pixel intensities from the background images were then subtracted from the images obtained with the flame operating.

4. EXPERIMENTAL SETUP

A brief description of the swirl burner is given here and more detail is available from Schneider et al. [26]. A cross-section of the burner is shown in figure 3, illustrating a 15 mm wide annular slot that surrounds a 30 mm wide central bluff-body. The fuel gas (methane) is premixed with the combustion air in the main body. The mixture passes through the swirl inducer and exits the nozzle through the 15 mm annular slot. The volume flow rate of the air co-flow was 900 l/min. The flow conditions

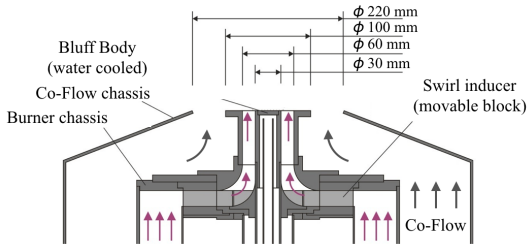

Fig. 3. Swirl burner cross-section.

used are summarised in table 1. The flow rate of all the gases was controlled using Bronkhorst mass flow controllers. Two equivalence ratios were considered, ϕ = 1.0 and 0.83. In both cases the methane flow was fixed at 50 l/min, while the air flow rate was 500 l/min (to achieve ϕ = 1.0) and 600 l/min (to achieve ϕ = 0.83), resulting in a cold flow Reynolds number of Re = 12,885 and Re = 15,457 respectively, based on the bluff-body diameter. The burner was run with an effective swirl number of S = 0.5 (Flame I and II), which has been the standard configuration in our laboratory as also investigated by Röder et al. [22]. An additional LES simulation was made with S = 0.75 (Flame III) only for the phantom study, for validation of the CTC algorithm, as detailed in section 5. The bulk of the study in this paper considers Flame I and II. The burner head temperature was 60°C.

Table 1. Swirl burner flow conditions tested. ϕ is the equivalence ratio, $\dot{V}_{CH_4}$ and $\dot{V}_{Air}$ are the methane and air volume flow rates of the reacting mixture respectively, S is the swirl number, Re is the cold flow Reynolds number and t_{exp} is the camera exposure time used for obtaining the flame images.

Case	ϕ	$\dot{V}_{CH_4}$ (m^3/h)	$\dot{V}_{Air}$ (m^3/h)	S	Re	t_{exp} (ms)
Flame I	1.00	3	30	0.5	12,885	0.4
Flame II	0.83	3	36	0.5	15,457	0.4
Flame III	0.83	3	35	0.75	10,000	0.5

The emission from thermally excited water (in the red and the near-infrared wavelength region) that was detected in the post-flame region from initial tests resulted in blurred images as shown in figure 4. The most intense chemluminescence originates from zones close to the flame front. However, hot H_2O is present in the exhaust gases and contributes interfering signal with a different spatial distribution. Therefore, it was critical to place an appropriate optical filter in front of the cameras to suppress the water emission. Considering the spectral response of the cameras, the Schott BG40 coloured glass filter was found to be the most suitable since it suppressed the water emission as shown in figure 5, but transmitted adequate signals so the flame could still be seen. Examples of the instantaneous and time-averaged (from 100 snapshots) images of Flame I and II, for both equivalence ratios and with S = 0.5, are presented in figure 6. As shown, the flame is highly turbulent and has a distinctly different shape in each case. The flame exhibits an M-shape and spreads over a larger spanwise region when ϕ = 1.0, but it is confined to a narrower region and has a V-shape when ϕ = 0.83.

The swirl flame has been subject to numerous investigations including Freitag et al.'s [21] and Jones et al.'s LES studies [27], and a similar flame shape as seen here is exhibited by the relevant papers [27–29]. According to Butz et al. [23], the reacting flow's mean axial and azimuthal velocity profile, for ϕ = 0.83 and S = 0.75, peaks at approximately 6 m/s. This means, that in the worst case, with a camera exposure time of t_{exp} = 0.4 ms an estimated image blurring over 2.4 mm exists in the region with the highest flow speed within the experimental images, due to the shift of luminous zones during camera exposure.

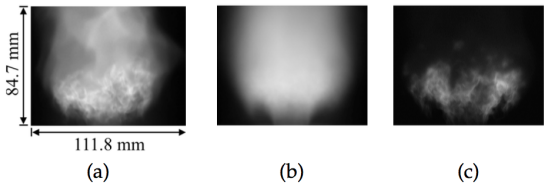

Fig. 4. Examples of (a) instantaneous and (b) time-averaged experimental images of the swirl Flame I (ϕ = 1.0) without water-suppression filters in front of the cameras, and (c) instantaneous image with the Schott BG40 filter. Camera exposure time is t_{exp} = 0.4 ms.

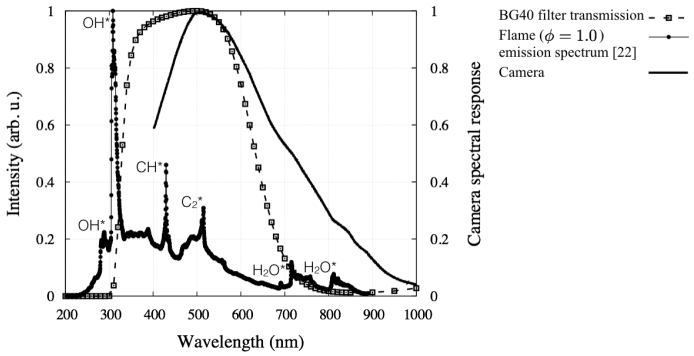

Fig. 5. Spectral response of the cameras, transmission curve of the Schott BG40 filter used for water emission suppression, and the swirl Flame I (ϕ = 1.0) emission spectrum [22].

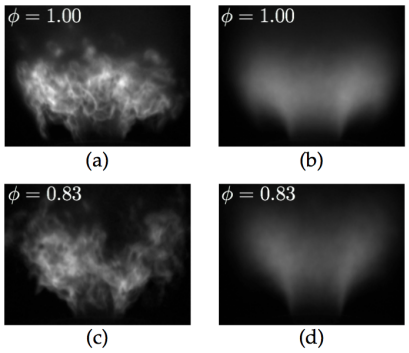

Fig. 6. Examples of camera views for the stoichiometric Flame I (a, b) and the lean Flame II (c, d), showing instantaneous snapshots (a, c) and time-averages (b, d). Camera exposure time is t_{exp} = 0.4 ms.

5. VALIDATION OF THE CTC ALGORITHM USING AN LES PHANTOM

In order to validate that our CTC algorithm can reconstruct the highly turbulent swirl flame's 3D shape, we performed a phantom test. We generated a phantom that represents the swirl

flame by LES of the flame using our in-house code PsiPhi [30, 31] (a highly accurate and massively parallel code for LES and DNS with combustion). The code has been applied to a range of cases such as stratified flames [32] and spray flames for the synthesis of nanoparticles [33].

To ensure that the LES phantom could be validated by existing experimental data in the literature, we performed the simulations using the same flow conditions used in the relevant papers [23, 26, 34] (given in table 1 as Flame III: ϕ = 0.83, S = 0.75 and cold flow Re = 10,000). The simulations were performed using over 30 million cells. The total computational time was 50,000 core hours, for a real time of 1.6 s. Combustion was modeled using the premixed flamelet generated manifold (FGM) approach that is coupled with the artificial flame thickening (AFT) method, as implemented in our code by Proch et al. [32]. The results (radial profiles of the mean and rms axial velocity, and the mean temperature) were compared with the experiments by Schneider et al. [26] and Gregor et al. [34], and with the simulations of Butz et al. [23]. The recirculation zone of the flame at the centreline and the flame shape were predicted well with our simulations.

Based on the agreement between our LES data and the experimental results, we concluded that our 3D LES data provides a sufficient representation of the turbulent swirl flame, and can be used as a phantom to validate our CTC algorithm. The source term field of the transport equation for the progress variable, which describes the creation of H_2O, CO_2 and H_2, was used to generate the 3D phantom field. The source term represents the heat release, which can be assumed to be sufficiently close to the broadband chemiluminescence field of the flame to permit a comparison of the geometry of the turbulent premixed flame burning in the flamelet regime. It must be noted that if the emission intensities of the phantom are to be quantitatively linked to the experiment the relevant reactions, which are only partially known with a high uncertainty in their rate constants, would need to be considered.

Projections of the phantom were generated, at the same 24 camera locations as in the tomography experimental setup, and assuming an ideal lens with no distortion, beam steering or image noise effects. Therefore, the phantom reconstruction is a pure test of the algorithm alone. The phantom was reconstructed using these projections and the original and reconstructed phantoms were compared by calculating the normalised Euclidean distance between them. The horizontal slices (normal to the views) from the original and reconstructed phantoms, at different heights above the burner are presented in figure 7. Looking at the horizontal planes is important and allows for a more critical assessment of the reconstruction quality, as explained in sub-section B. The heights are normalised to the burner's bluff-body diameter D_T = 30 mm. The reconstruction error was quantified by the normalised Euclidean distance ϵ, similar to [35], and is expressed by

$$\epsilon(Q) = \frac{||Q^{exact} - Q||_2^2}{||Q^{exact}||_2^2} \quad (2)$$

Where Q^{exact} and Q are the original and reconstructed phantoms respectively. The mean normalised Euclidean distance ϵ_{mean} was calculated for different horizontal slices at different heights above the burner, for a population of 10 different phantoms, and presented in figure 8. The standard deviation error bars are also shown. We note that on average, ϵ_{mean} increases with height above the burner, indicating larger deviations from the perfect reconstruction. This is attributed to the increased complexity in the flame structure, increased wrinkling, which poses a bigger challenge on reconstructions further downstream.

In addition to the phantom study, the reproducibility of our CTC technique, and adequacy of the camera alignment method used here, was checked by reconstructing the 21 jets of a matrix burner, and comparing to the previous reconstructions of the same burner by Floyd et al. [12].

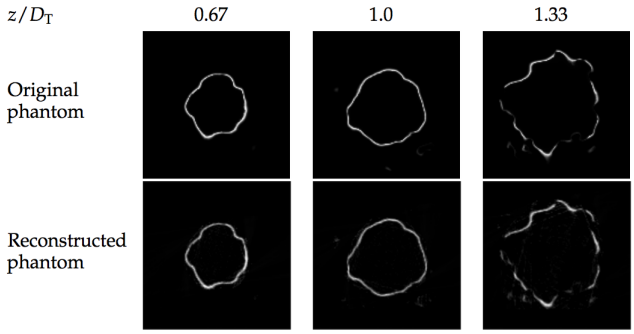

Fig. 7. Horizontal slices from the original and reconstructed phantom heat release field for the swirl Flame III, at different heights z above the burner, relative to the bluff body diameter D_T.

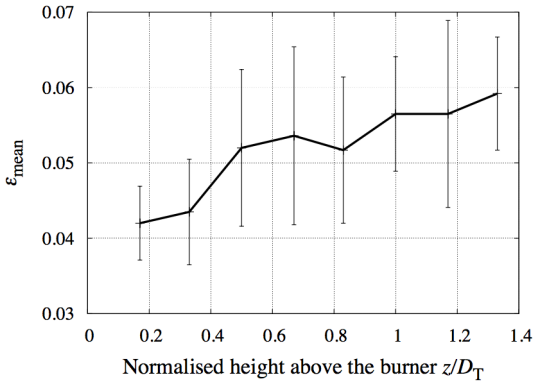

Fig. 8. Mean normalised Euclidean distance ϵ_{mean} of reconstructed phantoms compared to the original phantoms, for horizontal slices at different heights z/D_T above the burner. Data is presented for a population of 10 different Flame III phantoms, with standard deviation error bars.

6. DETAILED RECONSTRUCTIONS OF THE SWIRL FLAME I AND II

The 3D chemiluminescence field of the swirl Flame I and II was reconstructed using all 24 views. The experimental views were 190 by 144 pixels in the horizontal and vertical directions. This provided a total of N_p = 27,360 projection measurements per view, and a total of 656,640 equations. The pixel resolution in the flame views was 0.3 mm. The 3D reconstruction domain constituted 190 by 190 by 144 voxels in the xyz directions, forming a total of N_v = 5,198,400 voxels (unknowns). The coordinate systems are defined in figure 1.

As expected, the measurements benefit from stronger signals for ϕ = 1.0 compared to ϕ = 0.83. The horizontal slices obtained from the 3D reconstructed chemiluminescence field of the instantaneous and time-averaged flame (from 100 instantaneous

images), at different heights above the burner, are presented in figure 9 for both ϕ cases. It can be seen that the reconstruction resolution is good, suffering from minimal line-artefact pollution, most likely due to the large number of $N_q = 24$ views used. The reconstructed field for Flame I is rotated around in the movie file provided (Visualisation 1), to illustrate the flame geometry detail. Vertical slices (parallel to the views) are shown at the flame centreline, $x = 0$, and at two further vertical planes in close vicinity of the centreline in figure 10, exposing more of the instantaneous asymmetric flame shape.

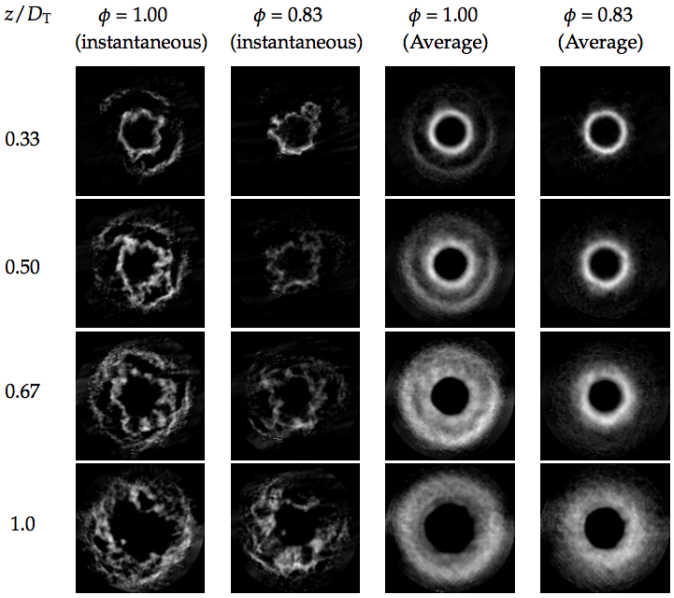

Fig. 9. Horizontal slices from the 3D reconstructed chemiluminescence field of the instantaneous and averaged swirl Flame I and II ($\phi = 1.0$ and $\phi = 0.83$, respectively), at different heights z above the burner, relative to the bluff body diameter D_T.

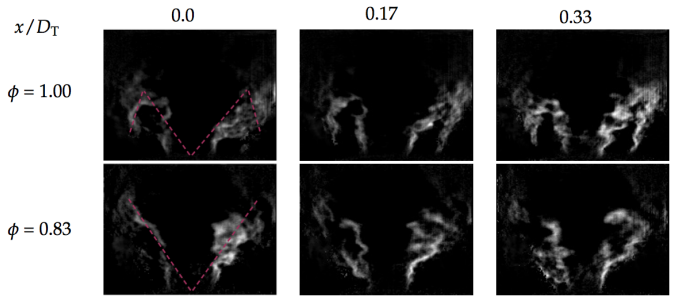

Fig. 10. Vertical slices from the 3D reconstructed chemiluminescence field of the instantaneous swirl Flame I and II ($\phi = 1.0$ and $\phi = 0.83$, respectively), at the flame centreline $x/D_T = 0$ and two neighbouring vertical planes. The dotted lines illustrate the M and V flame shapes.

The raw flame images already exhibited an M-shape for $\phi = 1.0$ compared to a V-shape for $\phi = 0.83$. The reconstruction data presented in figures 9 and 10 confirm this observation. Furthermore, considering the line-of-sight nature of the chemiluminescence measurements, the data unveils detailed flame structures in the horizontal planes which could not be directly accessible with the experimental images. As the instantaneous slices in figure 9 and figure 10 illustrate, the flame wrinkling increases with increasing height above the burner. This is in agreement with the LES data of Jones et al. [27] who report that the flame ($\phi = 0.83$) close to the nozzle exit is virtually flat with little wrinkling and expands with increased wrinkling further downstream.

Based on their LES data, Butz et al. [23] postulate that due to the radial flapping motion of the main reactant stream, burnt products sporadically seep into the outer rim of the flame, towards the co-flow, and can reside there due to the low co-flow velocity. They also point out that the flame does not seep in the radial direction on the inner flame region due to the fast main stream that washes away any such occurrences. In agreement with Butz et al., for $\phi = 1.0$ the reconstructions demonstrate that the flame distinctly penetrates into the slow co-flow region (0.5 m/s), and folds down around the rim towards the burner to form a three-dimensional M-shape. This can be inferred from closer inspection of the horizontal plot at $z/D_T = 0.33$ and 0.5 (first two rows in figure 9), where two main flame fronts are seen. Although the cold reactant flow in the $\phi = 0.83$ case is faster than for $\phi = 1.0$, in the reactive case the $\phi = 1.0$ flame is hotter and has a higher laminar flame speed (S_L), and thus can spread more in the radial direction. Reconstructions of the averaged flame illustrate that the expected cross-sectional ring shape of the flame's inner core close to the burner exit has been almost perfectly reproduced.

A. Effect of number of views

The reconstruction data presented so far involved using all the 24 views. In this section the extent of loss in reconstruction quality using our CTC technique with decreasing numbers of views N_q will be presented. The swirl Flame I ($\phi = 1.0$) was chosen as the test-case for this study.

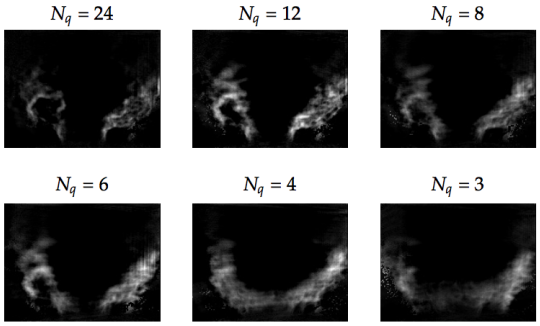

Fig. 11. Vertical slices from the 3D reconstructed chemiluminescence field of the instantaneous swirl Flame I ($\phi = 1.0$), at the flame centreline $x/D_T = 0$, using different numbers of views N_q.

Flame I was reconstructed with progressively less numbers of views, but maintaining their constant angular separation, i.e., equally spaced within the 172.5° region in one plane around the flame. Figures 11 and 12 show examples of the resulting reconstructed vertical and horizontal slices, respectively. The results demonstrate that, as expected, reducing the N_q results in diminishing clarity of flame structures. The horizontal slices show further that line-artefacts increasingly pollute the reconstructed field. The emergence of these artefacts depends on the ratio of the number of voxels to the number of projections (equations). This issue will be discussed in more detail in sub-section D. Based on previous experience [18], the appearance of the artefacts is also likely to weakly depend on the geometry that is reconstructed.

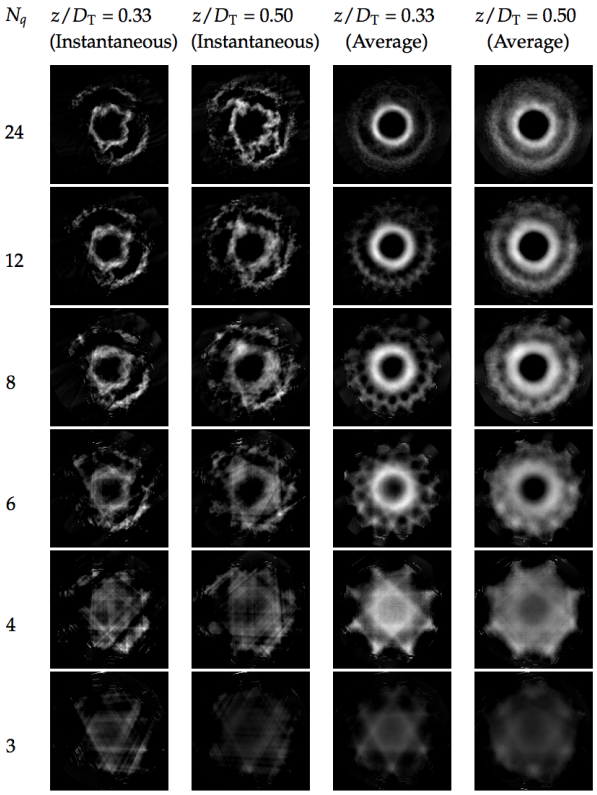

Fig. 12. Horizontal slices from the 3D reconstructed chemiluminescence field of the instantaneous and averaged swirl Flame I (ϕ = 1.0), at two different heights above burner z/D_T, using different numbers of views N_q.

The correlation of the horizontal and vertical slices for all the lower N_q cases with the equivalent slice from the N_q = 24 case was calculated (considering the N_q = 24 as the best reconstruction case), for several distances above the burner and several vertical planes. It must be noted that the 24-view reconstruction is not free of errors, however, it is used as a reference since it includes our best available knowledge of the flame. The correlation represents the similarity between each set of two slices with reference to their respective pixel intensities. Examples of the correlations, which increase with larger N_q for all cases, are presented in figure 13.

B. Assessment of 3D reconstructions

The volumetric reconstructions can be assessed in various ways such as observing the 3D field from arbitrary angles or cutting slices from different orientations. Various approaches are demonstrated in the literature such as relying more heavily on studying the vertical slices that are parallel to the measured views [17, 36] or also considering the horizontal slices that are normal to the measured views [8, 10, 12].

From figures 11 and 12 it is clear that the decline in reconstruction quality with reduced N_q does not seem as substantial when observing only the vertical slices. For example, for the N_q = 4 case the vertical slice at the flame centreline in figure 11 appears to show a relatively reasonable reconstruction, whereby the overall flame structure is still visible. However, with the same N_q the horizontal slice in figure 12 shows a much poorer representation of the flame structure that is crowded with line-artefacts, making

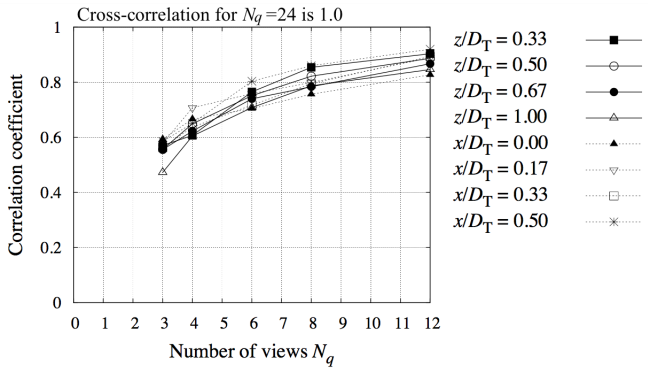

Fig. 13. Correlation of the 3D reconstructed chemiluminescence field horizontal and vertical slices of the instantaneous swirl flame I (ϕ =1.0) using different numbers of views N_q at several heights above the burner z/D_T and vertical planes x/D_T, with the corresponding slice from the reconstruction using 24 views.

it difficult to distinguish where the flame actually is. The view-normal (horizontal) slices are usually more difficult to resolve (in most flames) than view-parallel (vertical) slices. In some recent work we have noticed that view-parallel planes have been presented for reconstructions of simple slot flames, where we believe that a processed single-camera image could also present a reasonable reconstruction view-parallel slice. However, our study shows that to assess the true performance of the algorithm and quality of reconstructions, inspecting the view-normal slices of the reconstructed field must not be overlooked.

In figure 14 some of the original views are compared to projections from the reconstruction using 24 views at exactly the same view angles that were used for the reconstructions. Projections from the reconstruction using 4 views are also shown, once at the same view angle that was used for the reconstruction and once not at an angle that corresponds to an original view. The images in this figure clearly demonstrate that when comparing projections to an original view at the same angle the results will grossly overestimate the real resolution of the reconstruction - a common problem in some recent papers on flame chemiluminescence tomography. However, a camera that has not been used for the reconstruction may be utilised to provide a suitable estimate of the reconstruction quality.

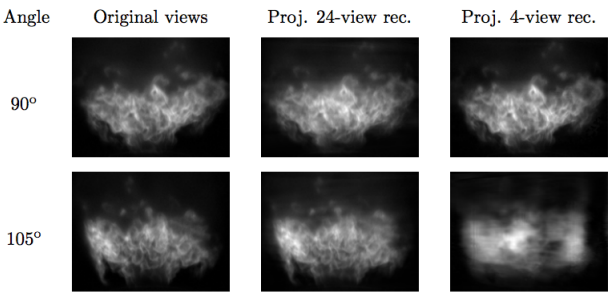

Fig. 14. Original views compared to projections from the reconstructions using 24 views and 4 views, for all reconstructions at matching view angles (top row), and at a different view angle for the 4-view reconstruction (bottom row).

C. Effect of the views' spatial variation, in one plane

The swirl Flame I reconstructions were repeated by varying the angular separation $\Delta\theta$ between the measured views. The spatial variance σ^2 in $\Delta\theta$ was quantified by the following expression:

$$\sigma^2 = \sum_{i=1}^{N_q-1} \frac{(\Delta\theta_i - \overline{\Delta\theta})^2}{N_q - 1} \quad (3)$$

In equation 3, $\overline{\Delta\theta}$ is the mean angular separation. The spatial variation was increased by choosing random sets of cameras from the original set and not by moving individual cameras. Considering the reconstruction using 24 views as the best case again, the correlation of the horizontal slices for all the lower N_q data with the equivalent slice from the reference case ($N_q = 24$, $\sigma^2/(\overline{\Delta\theta})^2 = 0$) was calculated for all the spatial variances that were considered. The results are presented in figure 15 for different heights above the burner. The data support the hypothesis that the correlation reduced with increased spatial variation, especially further downstream of the burner (i.e., for $z/D_T \geq 0.67$).

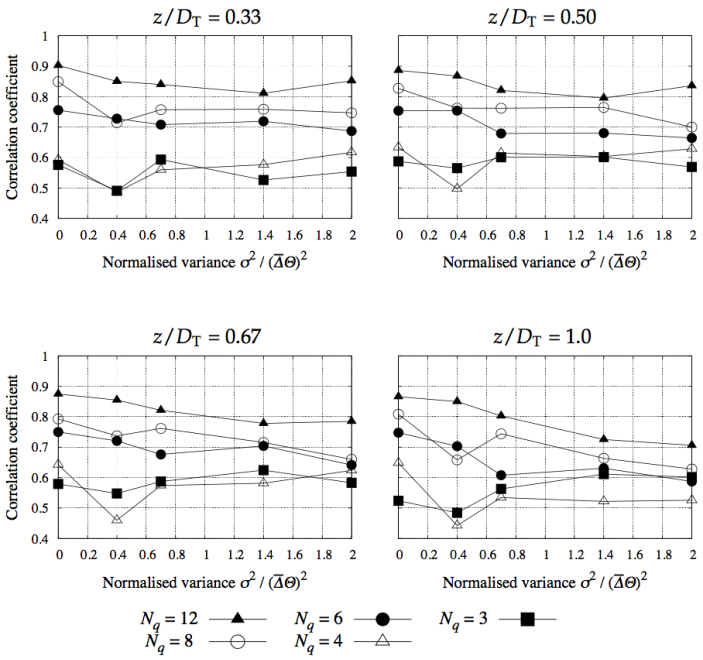

Fig. 15. Correlation of the 3D reconstructed chemiluminescence field horizontal slice of the instantaneous swirl Flame I ($\phi = 1.0$) using different view spatial variances $\sigma^2/(\overline{\Delta\theta})^2$, for different numbers of views N_q, with the corresponding reconstructed slice using 24 views ($\sigma^2/(\overline{\Delta\theta})^2 = 0$). Plots are presented for different heights above the burner z/D_T.

D. Effect of the number of voxels in the reconstruction domain

The system of linear equations that is generated by discretising the flame domain into a total number of N_v voxels (containing as many rows as there are total measured projections $N_p \times N_q = N_{pq}$, and as many columns as there are unknown values N_v) is mathematically ill-posed [24, 37]. Furthermore, depending on the density of data sampling, the system may be under-determined (rank-deficient) or full-rank [24, 35]. In the majority of our reconstructions the system is rank-deficient, as shown in figure 16, where $N_v > N_{pq}$. It should be noted that in the few cases where the full-rank condition seems to be achieved, for the lowest N_q values ($N_v \leq N_{pq}$), the system in reality is still most likely rank-deficient due to overlapping rays from the projections. For the $N_q = 24$ case, the ratio of the maximum number of voxels $N_{v,o}$ to the total number of projection measurements is $N_{v,o}/N_{pq}$ =7.9, and for the $N_q = 3$ case the ratio is $N_{v,o}/N_{pq} = 63$. We investigated the effect of reducing N_v on the reconstructions, for the swirl Flame I ($\phi = 1.0$).

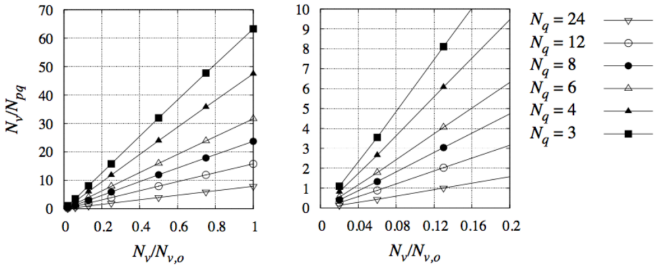

Fig. 16. Relationship between the ratio of number of voxels to number of projections N_v/N_{pq} and the normalised number of voxels $N_v/N_{v,o}$ for the different N_v cases tested. $N_{v,o}$ is the maximum number of voxels used in the reference case. Data is shown for all the different number of views N_q considered.

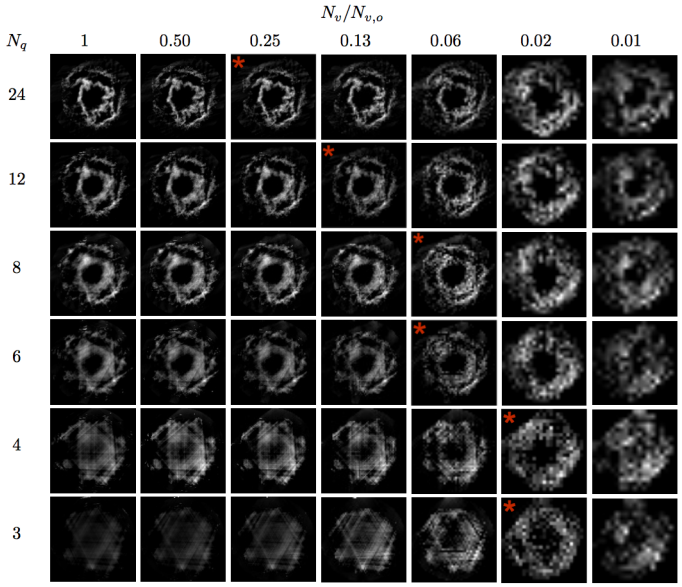

Fig. 17. Horizontal slices at $z/D_T = 0.5$ from the 3D reconstructed chemiluminescence field of the instantaneous swirl Flame I ($\phi = 1.0$), for different number of voxels N_v normalised by the maximum value $N_{v,o}$, and different numbers of views N_q. The star indicates the best reconstruction in our opinion.

The swirl Flame I ($\phi = 1.0$) was reconstructed using progressively less voxels such that $N_v < N_{v,o}$, for all the N_q cases. Several N_v values were tested, and figure 16 shows the relationship between the ratio of N_v/N_{pq} and the normalised number of voxels tested for each N_q case. Each line on the graph represents a specific N_q. Examples of the resulting reconstructed horizontal slices at $z/D_T = 0.5$ are presented in figure 17. It appears that as $N_v/N_{v,o}$ is lowered, for the maximum $N_q = 24$ case the reconstructions seem to loose quality, whilst for the lowest $N_q = 3$

case the general flame structure appears to be recovered better. Based on a visual inspection of the slices shown in figure 17, we qualitatively deduce that an optimum value of $N_v/N_{v,o}$ for each N_q seems to exist, and have indicated this by the *.

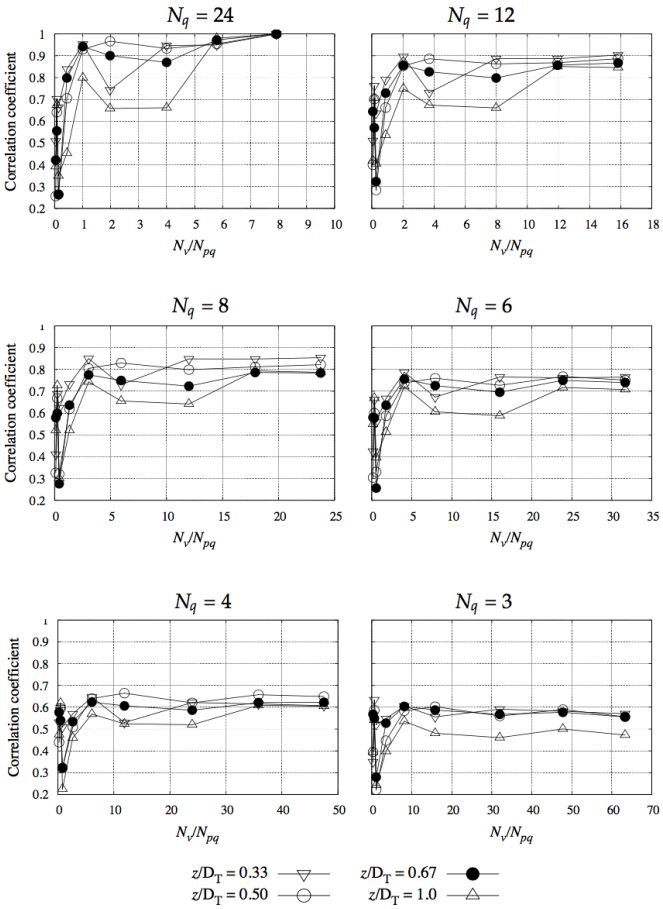

Fig. 18. Correlation of the 3D reconstructed chemiluminescence field horizontal slices of the instantaneous swirl Flame I (ϕ = 1.0) using different numbers of views N_q, for different reconstruction domain voxels N_v normalised by the total measured projections N_{pq}, with the reference cross-section using 24 views. Plots are presented for different heights above the burner z/D_T.

To quantify the effect of N_v on the reconstructions it was appropriate to calculate the correlation between all the cross-sectional slices for different N_v cases and one chosen reference cross-sectional slice. The cross-section from the reconstruction using N_q = 24 and $N_{v,o}$ was chosen as the reference. Since different numbers of voxels were used in this study, the cross-sectional slices for different N_v cases actually contain a different number of pixels. Therefore, to make the slice sizes compatible for all the N_v cases we chose to down-sample the fine reconstruction from the reference slice (which had the largest number of pixels), using bicubic interpolation, rather than up-sampling the coarser reconstructions. We believe that removing some information is less questionable than generating new information through interpolation. The correlation, based on the respective pixel intensities of each two sets of horizontal slices was calculated, and the results are plotted in figure 18.

The correlations are plotted against the ratio of N_v/N_{pq}. The results for each N_q case are shown on a separate graph, for better clarity. The overall correlation is highest for the highest N_q, for which $(N_v/N_{qp})_{max} < 8$ when $N_v/N_{v,o} = 1$, from figure 16. When N_v/N_{pq} was lowered the correlations for the highest N_q = 24 case dropped, whilst for the N_q = 3 case the correlations show the opposite effect. The remaining N_q cases in between show an intermediary behaviour between these two extremes. Based on this observation, it can be argued that in the most sparsely sampled cases, e.g. when N_q = 3 and N_q = 4, decreasing the total number of unknowns N_v, or voxels, actually aids the system to generate better results. In the small region where $N_v \leq N_{pq}$ the correlations appear to exhibit an unsteady behaviour. As explained earlier, although the system is formally full-rank in these cases, it is still not a guarantee that all the equations (formed by the measured projections) are linearly independent due to overlapping rays. An extended study will be needed to investigate this aspect.

7. CONCLUSIONS

The instantaneous 3D chemiluminescence field of a realistic, premixed swirl flame was reconstructed with the CTC technique, for the first time. A maximum number of 24 views, equiangularly distributed in a 172.5^o region in one plane around the flame were used to reconstruct the instantaneous and time-averaged flames. The reconstructed instantaneous fields unveiled structural detail in the cross-sectional slices with relatively high clarity, and revealed different flame geometries for the different equivalence ratios when the swirl number is S = 0.5. For ϕ = 1.0, the flame seeps into the surrounding co-flow, and folds around the rim towards the burner to form an M-shape that is highly asymmetric in the instantaneous views. For ϕ = 0.83, the flame speed is too low for folding around, an M-shape cannot evolve and the flame burns in a V-configuration.

An additional validation of the algorithm, beyond the work of Floyd et al. [12], was conducted for a steady matrix burner and an LES phantom of the swirl flame, which confirmed repeatability of the CTC technique and that the method of camera alignment used in the current work was adequate. We have highlighted that to determine the true quality of reconstructions both view-normal and view-parallel slices of the reconstructed field must be considered. Furthermore, when comparing projections from the reconstructions to an original view at the same angle, the reconstructed view can be expected to agree very well with the original view, so that such a comparison must not be used to infer quality and resolution of the reconstructions. This effect has been unfortunately ignored in several recent papers, that claimed unrealistically high resolutions in otherwise excellent work.

The results confirmed that in general it is best to arrange the cameras, that populate a semicircle around the flame in one plane, equiangularly. We have shown that too few views (knowns) and too many voxels (unknowns) lead to a poorly conditioned algebraic system - visible in our reconstructions as line artefacts. With a suitably reduced number of voxels, the quality of reconstruction does however deteriorate in a benign manner if the number of views are reduced, keeping the reconstructions very useful, just with less detail. Even a small number of views (e.g. 4) appears to be sufficient to observe larger asymmetries in the flame - like those caused by coherent vortex cores or maybe even thermoacoustic fluctuations in the heat release.

8. ACKNOWLEDGEMENTS

The authors gratefully acknowledge the financial funding of the BMWi (03ET7011B), Siemens and the Ministerium für Innovation, Wissenschaft und Forschung des Landes Nordrhein-Westfalen. We thank Mr. O. Hasemann, Dr. J. Floyd and Mr. J. Verbeke for their support and many helpful discussions. We are also greatful for the computing time on magnitUDE (for the LES) from the Center for Computational Sciences and Simulation (CCSS) at the University of Duisburg-Essen (DFG grant INST 20876/209-1 FUGG, INST20876/243-1 FUGG), at the university's Zentrum für Informations-und Mediendienste (ZIM).

REFERENCES

1. L. D. Chiffre, S. Carmignato, J.-P. Kruth, R. Schmitt, and A. Weckemann, "Industrial applications of computed tomography," CIRP Annals **63**, 655–677 (2014).
2. A. K. Agrawal, N. K. Butuk, S. R. Gollahalli, and D. Griffin, "Three-dimensional rainbow schlieren tomography of a temperature field in gas flows," Appl. Opt. **37**, 479–485 (1998).
3. A. Schröder, R. Geisler, G. E. Elsinga, F. Scarano, and U. Dierksheide, "Investigation of a turbulent spot and a tripped turbulent boundary layer flow using time-resolved tomographic PIV," Exp. Fluids **44**, 305–316 (2008).
4. Y. Sivathanu, J. Lim, and R. Joseph, "Statistical absorption tomography for turbulent flows," J. Quant. Spectrosc. Radiat. Transfer **68**, 611–623 (2001).
5. B. R. Coriton, A. M. Steinberg, and J. H. Frank, "High-speed tomographic PIV and OH PLIF measurements in turbulent reactive flows," Exp. Fluids **55**, 1743–62 (2014).
6. X. Li and L. Ma, "Capabilities and limitations of 3D flame measurements based on computed tomography of chemiluminescence," Combust. Flame **162**, 642–651 (2015).
7. J. Wang, Y. Song, Z. Li, A. Kempf, and A. He, "Multi-directional 3D flame chemiluminescence tomography based on lens imaging," Opt. Lett. **40**, 1231–1234 (2015).
8. N. A. Worth and J. R. Dawson, "Tomographic reconstruction of OH* chemiluminescence in two interacting turbulent flames," Meas. Sci. Technol. **24**, 024013 (2013).
9. M. M. Hossain, L. Gang, S. Duo, and Y. Yong, "Three-dimensional reconstruction of flame temperature and emissivity distribution using optical tomographic and two-colour pyrometric techniques," Meas. Sci. Technol. **24**, 074010 (2013).
10. M. M. Hossain, L. Gang, and Y. Yong, "Optical fiber imaging based tomographic reconstruction of burner flames," IEEE Transactions on Instrumentation and Measurement **61**, 1417–1425 (2012).
11. N. B. Anikin, R. Suntz, and H. Bockhorn, "Tomographic reconstruction of 2D-OH*-chemiluminescence distributions in turbulent diffusion flames," Appl. Phys. B **107**, 591–602 (2012).
12. J. Floyd and A. Kempf, "Computed tomography of chemiluminescence (CTC): High resolution and instantaneous 3-D measurements of a matrix burner," Proc. Combust. Inst. **33**, 751–758 (2011).
13. J. Floyd, P. Geipel, and A. Kempf, "Computed tomography of chemiluminescence (CTC): Instantaneous 3D measurements and phantom studies of a turbulent opposed jet flame," Combust. Flame **158**, 376–391 (2011).
14. S. Wysocki, J. Floyd, and A. M. Kempf, "Efficient parallel tomographic reconstruction of chemiluminescence in flames," European Combustion Meeting (2011).
15. Y. Ishino and N. Ohiwa, "Three-dimensional computerized tomographic reconstruction of instantaneous distribution of chemiluminescence of a turbulent premixed flame," JSME Int J., Ser. B **48**, 34–40 (2005).
16. H. M. Hertz and G. W. Faris, "Emission tomography of flame radicals," Opt. Lett. **13**, 351–353 (1988).
17. L. Ma, Y. Wu, Q. Lei, W. Xu, and C. D. Carter, "3D flame topography and curvature measurements at 5 kHz on a premixed turbulent bunsen flame," Combust. Flame **166**, 66–75 (2016).
18. J. Floyd, "Computed tomography of chemiluminescence: a 3D time resolved sensor for turbulent combustion," Ph.D. thesis, Imperial College London (2009).
19. D. Mishra, J. P. Longtin, R. P. Singh, and V. Prasad, "Performance evaluation of iterative tomography algorithms for incomplete projection data," Appl. Opt. **43**, 1522–1532 (2004).
20. W. Meier, O. Keck, B. Noll, O. Kunz, and W. Stricker, "Investigations in the TECFLAM swirling diffusion flame: Laser raman measurements and CFD calculations," Appl. Phys. B **71**, 725–731 (2000).
21. M. Freitag, M. Klein, M. Gregor, D. Geyer, C. Schneider, A. Dreizler, and J. Janicka, "Mixing analysis of a swirling recirculating flow using dns and experimental data," Int. J. Heat Fluid Flow **27**, 636–643 (2006).
22. M. Röder, T. Dreier, and C. Schulz, "Simultaneous measurement of localized heat release with OH/CH2O-LIF imaging and spatially integrated OH* chemiluminescence in turbulent swirl flames," Proc. Combust. Inst. **34**, 3549–3556 (2013).
23. D. Butz, Y. Gao, A. Kempf, and N. Chakraborty, "Large eddy simulations of a turbulent premixed swirl flame using an algebraic scalar dissipation rate closure," Combust. Flame **162**, 3180–3196 (2015).
24. K. J. Daun, S. J. Grauer, and P. J. Hadwin, "Chemical species tomography of turbulent flows: Discrete ill-posed and rank deficient problems and the use of prior information," J. Quant. Spectrosc. Radiat. Transfer **172**, 58–74 (2016).
25. K. T. Walsh, J. Fielding, and M. B. Long, "Effect of light-collection goemetry on reconstruction errors in abel inversions," Optics letters **25**, 457–459 (2000).
26. C. Schneider, A. Dreizler, and J. Janicka, "Fluid dynamical analysis of atmospheric reacting and isothermal swirling flows," Flow Turbul. Combust. **74**, 103–127 (2005).
27. W. P. Jones, A. J. Marquis, and V. N. Prasad, "LES of a turbulent premixed swirl burner using the eulerian stochastic field method," Combust. Flame **159**, 3079–3095 (2012).
28. A. Nauert and A. Dreizler, "Conditional velocity measurements by simultaneously applied laser doppler velocimetry and planar laser-induced fluorescence in a siwrling natural gar/air flame," Z. Phys. Chem. **219**, 635–648 (2005).
29. G. Kuenne, A. Ketelheun, and J. Janicka, "LES modeling of premixed combustion using a thickened flame approach coupled with FGM tabulated chemistry," Combust. Flame **158**, 1750–1767 (2011).
30. C. Olbricht, J. Janicka, and A. M. Kempf, "Les as a prediction tool for lifted flames in a model gas turbine combustor," Proceedings of ASME Turbo Expo (2010).
31. M. W. A. Pettit, B. Coriton, A. Gomez, and A. M. Kempf, "Large-eddy simulation and experiments on non-premixed highly turbulent opposed jet flows," Proc. Combust. Inst. **33**, 1391–1399 (2011).
32. F. Proch and A. Kempf, "Numerical analysis of the cambridge stratified flame series using artificial thickened flame LES with tabulated premixed flame chemistry," Combust. Flame **161**, 2627–2646 (2014).
33. A. Rittler, L. Deng, I. Wlokas, and A. M. Kempf, "Large eddy simulation of nanoparticle synthesis from flame spray pyrolysis," Proc. Combust. Inst. (2017).
34. M. A. Gregor, F. Seffrin, D. Geyer, and A. Dreizler, "Multi-scalar measurements in a premixed swirl burner using 1d raman/rayleigh scattering," Proc. Combust. Inst. **32**, 1739–1746 (2009).
35. S. J. Grauer, P. J. Hadwin, and K. J. Daun, "Bayesian approach to the design of chemical species tomography experiments," Appl. Opt. **55**, 5772–5782 (2017).
36. X. Li and L. Ma, "Volumetric imaging of turbulent reactive flows at khz based on computed tomography," Opt. Express **22**, 4768–4778 (2014).
37. J. Hadamard, "Sur les problèmes aux dérivées partielles et leur signification physique," Princeton University Bulletin **13** (1902).